Review

Moh R. Amer*, Yazeed Alaskar, Hussam Qasem, Fadhel Alsaffar and Abdulrahman Alhussain

Integration of low-dimensional materials for energy-harvesting applications: current progress, scope, challenges, and opportunities

DOI 10.1515/ntrev-2016-0001
Received January 2, 2016; accepted February 16, 2016; previously published online July 27, 2016

Abstract: During the past few years, scientists have shown that climate change is a serious problem that mandates adequate solutions. Greenhouse gas emissions such as carbon dioxide contribute to heat trapping in the atmosphere, which increases the global temperature. Reducing greenhouse gas emissions and the carbon footprint to zero is an essential step toward maintaining a 2°C temperature change. In doing so, researchers and scientists have focused much attention on finding alternative technologies that provide clean and sustainable energy. In particular, nanotechnology can offer this alternative solution to the ongoing energy crisis. The recent progress in nanomaterial research has focused on the development of high-efficiency optoelectronics, batteries, low-power electronics, and thermoelectric devices for energy generation applications. With the emergence of new nanomaterials, such as carbonaceous materials and transition metal dichalcogenides, new physics have emerged. Scientists and engineers are still eager to answer some of the fundamental issues concerning these nanomaterials, including optical, electrical, and thermal properties. Yet, to this day, nanotechnology solutions to provide a sustainable energy are hinged by the ability to control and fully understand the properties of these nanomaterials. Here, we highlight some of the recent progress carried out in nano-optoelectronics, and share our thoughts on the opportunities and challenges facing low-dimensional devices to generate clean and sustainable energy.

Keywords: III-V semiconductors; organic photovoltaics; solar energy harvesting; tandem cell; thermoelectric devices; two-dimensional materials.

1 Introduction

Climate change has become a major global issue that requires immediate energy reliance from fossil fuel to clean and sustainable energy. Recent studies show that global warming is a serious threat to our planet and our existence [1, 2]. The effect of climate change in the next few decades will dramatically impact our global economy, agriculture, and spread of outbreak of diseases such as malaria [2]. Most notably, poor countries and low-income regions will suffer the most from climate change, mainly due to the inability of poor neighborhoods to recover from natural disasters, and crop failure due to reduced rainfalls. Unfortunately, we still depend on fossil fuel, which makes it not an easy task getting to zero greenhouse gas emissions. Current research and development are focusing on enabling new technologies that help shift our energy dependence to clean and sustainable energy.

In this article, we will focus on how nanotechnology enables promising solutions to this energy crisis. Mainly, we will highlight recent work in optoelectronics using various approaches for solar energy-harvesting applications. We aim to address the gap between low-dimensional devices and state-of-the-art performance. This article is divided into four sections. Section 1 reviews

***Corresponding author: Moh R. Amer,** Center of Excellence for Green Nanotechnologies, Department of Electrical Engineering, University of California, Los Angeles, CA 90095, USA,
e-mail: mamer@seas.ucla.edu; mamer@kacst.edu.sa; and Center of Excellence for Green Nanotechnologies, Department of Electrical Engineering, King Abdulaziz City for Science and Technology, Riyadh 11442, Saudi Arabia
Yazeed Alaskar and Hussam Qasem: Center of Excellence for Green Nanotechnologies, Department of Electrical Engineering, University of California, Los Angeles, CA 90095, USA; and Center of Excellence for Green Nanotechnologies, Department of Electrical Engineering, King Abdulaziz City for Science and Technology, Riyadh 11442, Saudi Arabia
Fadhel Alsaffar and Abdulrahman Alhussain: Center of Excellence for Green Nanotechnologies, Department of Electrical Engineering, King Abdulaziz City for Science and Technology, Riyadh 11442, Saudi Arabia

recent progress to produce efficient solar cells using two junctions, followed by recent progress on organic photovoltaics (OPVs). Section 2 discusses recent optoelectronic devices based on carbonaceous devices, in particular graphene and carbon nanotube solar cells and photodetectors. Section 3 undertakes the opportunities and challenges for the next generation of two-dimensional (2D) photovoltaics and thermoelectric devices. Finally, we conclude and provide our future outlook in Section 4.

1.1 III-V semiconductors on silicon for optoelectronics applications

Silicon technology is one of the remarkable achievements the last century has witnessed. Due to the abundance of silicon material, the extraordinary silicon properties, and the significant advancement in silicon lithography processes, various large-scale electronics can be easily realized. Extremely fast and reliable computer and mobile phone processors are becoming a reality, where, >20 years ago, personal computers and smart phones were a dream. Thanks to the scientific advancement in silicon technology, silicon electronics have enabled us to virtually communicate with anyone around the globe with just click of a button.

Silicon-based solar cells, however, cannot achieve >25% conversion efficiency. Mainly because silicon can only cover a small portion of the solar spectrum, rendering the rest of the spectrum untouched. Therefore, a new integrable approach to efficiently use the entire spectrum is required.

III-V materials such as gallium arsenide (GaAs) and gallium nitride (GaN) are widely integrated for optoelectronic applications. Ideally, integrating these semiconductor solar junctions on silicon solar junction is an intriguing method. However, due to the noticeably large lattice mismatch between III-V materials and silicon, integration of photovoltaics based on III-V semiconductors on silicon wafers has been a staggering challenge. It is desirable to have a junction that spans the entire solar spectrum, which spans from ultraviolet to near infrared. However, use of multiple junctions, or tandem cell, is one practical approach to cover this solar spectrum, where each junction is designed for a specific spectrum range, thus contributing to the total current. To date, the highest reported efficiencies using four solar junctions are 38% and 46% for non-concentrated and concentrated illuminations, respectively [3, 4].

The downside of this multijunction approach is the expensive cost of the growth technique and the substrate along with the limited choice of materials. Also, the design of multijunction devices requires current matching in order to achieve the highest efficiency acquired, which imposes another challenge in the fabrication of solar junction.

One approach to tackle the silicon lattice mismatch is to grow vertical nanowires on top of silicon *pn* junctions. Due to their low dimensionality, nanowires can overcome the lattice mismatch by strain relaxation at the edges. For instance, GaAs nanowires can be grown using the metalorganic chemical vapor deposition (MOCVD) technique. Doping of MOCVD-grown GaAs nanowires can be controlled by modifying the gas flow rate. In Figure 1A and B, the GaAs nanowire tandem cell and the scanning electron microscopy (SEM) image of as-grown GaAs nanowires are shown, respectively. In order to obtain the maximum possible current, a low-resistance connecting junction is required between the nanowire and the silicon junctions.

A recent attempt to fabricate high-efficiency tandem solar cells using GaAs nanowires on top of silicon *pn* junctions have shown satisfactory results. Yao et al. measured efficiencies close to 11.4% for these two junctions [5]. In Figure 1C, the measured current-voltage characteristics of the tandem cell are shown along with each stand-alone junction under the AM 1.5 G solar spectrum. The obtained current density for the tandem cell is 20.64 mA/cm^2, with open-circuit voltage of 0.956 V and fill factor of 0.578.

The integration of GaAs nanowire junction with silicon junction is aimed to produce efficiencies close to or higher than the Shockley-Queisser limit. In fact, the simulated result should exceed the silicon solar cell efficiency. The advantage of this technique is in the fabrication processes, where a SiN mask is used to pattern the GaAs nanowires, making it easy to grow controlled diameter nanowires. However, the low 11.4% efficiency measured for the tandem cell indicates major constrains. First, the design should optimize each junction parameter separately in order to obtain conversion efficiencies close to the theoretically predicted efficiency of each cell. In light of this, the GaAs nanowire junction lacks a concrete doping characterization method, although photoluminescence measurement is a viable approach. Also, defect states and other non-radiative recombination states should be handled with care. A careful choice of the passivation layer can reduce such non-radiative recombination states, which is absent in Figure 1A. Secondly, a low-resistance connecting junction between the nanowire junction and the silicon junction is required in order to obtain the maximum conversion current.

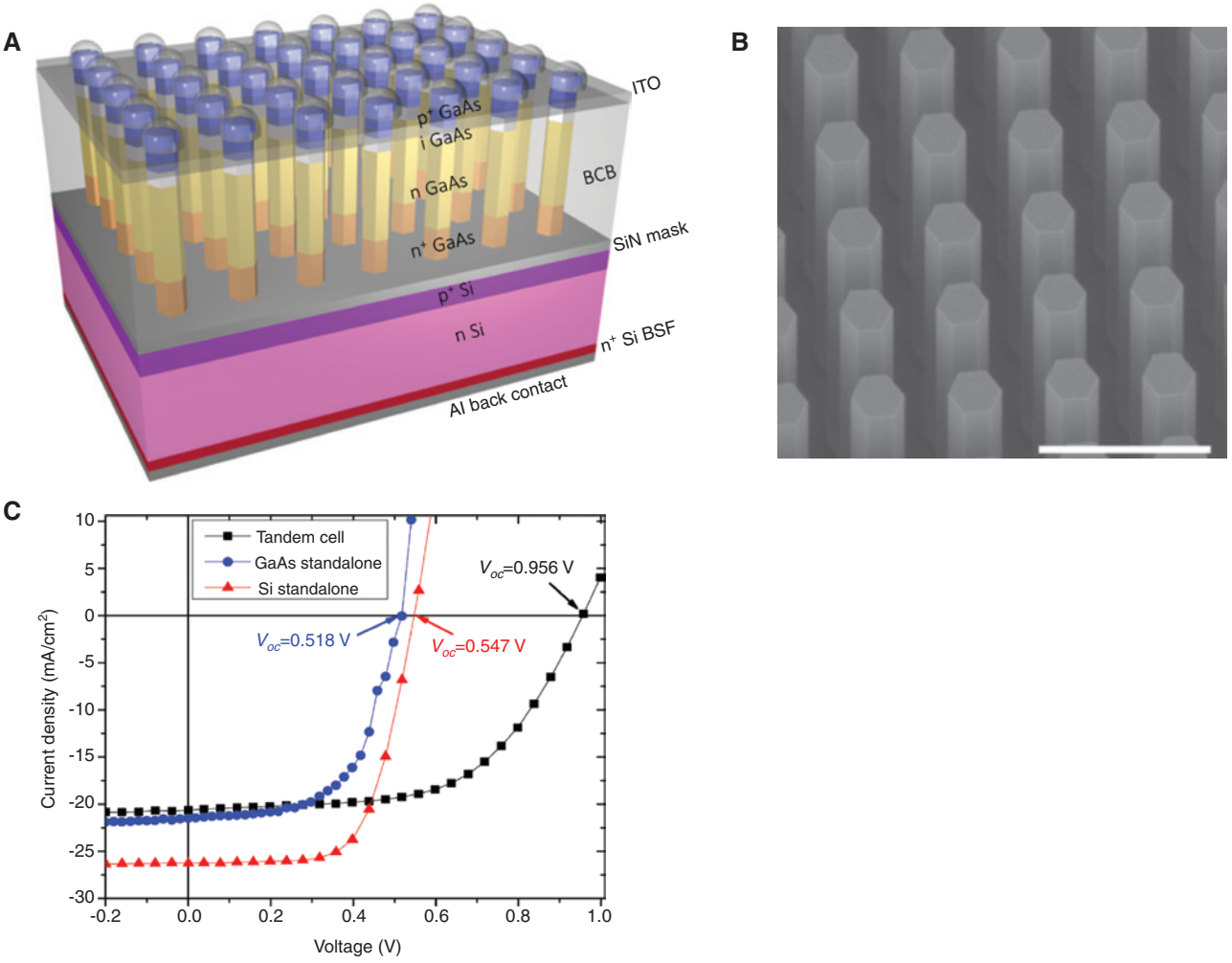

Figure 1: (A) Schematic diagram of the GaAs nanowire on silicon tandem cell. (B) SEM image of the grown GaAs nanowires showing high growth yield. The scale bar is 1 μm. (C) Measured current-voltage characteristic of the GaAs nanowire junction (blue circles), silicon junction (red triangle), and tandem cell (black square). The measured open-circuit voltage is approximately the summation of the open circuit current of both junctions [5].

Although this measured efficiency is low, this proof-of-concept tandem cell is a promising approach to obtain efficiencies that can surpass the Shockley-Queisser limit with two junctions.

Another promising approach to solve the lattice mismatch between III-V semiconductors and silicon is the inclusion of a buffer layer. That is, a 2D layer on silicon connected to the III-V material by van der Waals epitaxy can alleviate the lattice mismatch problem [6]. van der Waals epitaxy is advantageous in the sense that the stress caused by the lattice mismatch can be relaxed due to weak bonds at the interface between 3D/2D. The choice of this layer is crucial in order to prevent instability of the grown III-V semiconductor and ensure the sticking of the material on top of the 2D layer.

Figure 2A and B demonstrate this approach where graphene is used as the buffer layer between III-V semiconductors, in this case GaAs, and the silicon substrate. Here, graphene was used due to its thermal stability, which can accommodate high growth temperatures. GaAs was grown using molecular beam epitaxy with different growth parameters. The top graphene layer is under strain in order to lattice match the bulk GaAs layer. The final structure is expected to produce high-quality GaAs grown on silicon substrate, as illustrated in Figure 2B.

Although this is a viable approach to III-V semiconductors on silicon, there are still major challenges that hinder the fabrication of optoelectronics using this approach. One major issue is the limitations of the buffer layer between the silicon and the III-V semiconductor. That is, the surface energy of the 2D material layer can be low, which tends to produce island growth of GaAs on graphene instead of a uniform GaAs film [6]. Thus, the ability to control the growth sites is still open for research.

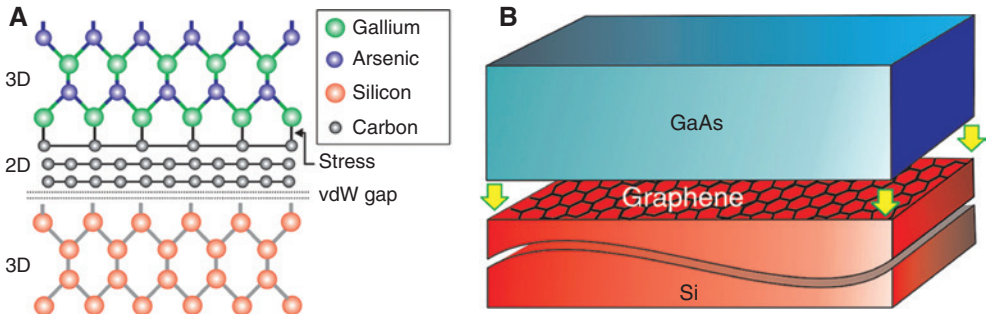

Figure 2: (A) Atomic diagram of the GaAs/multilayer graphene/silicon layers. (B) Visual representation showing the stacking of the GaAs/graphene/silicon layers [6].

Moreover, the stability of the grown GaAs on top of the buffer layer is of a noticeable concern. This is because the adsorption energy of Ga and As on graphene is pretty low, although an ultra-smooth GaAs surface has been achieved on graphene/silicon substrate using optimized growth parameters, as shown in Figure 3A and B. Producing high-efficiency GaAs solar cells on silicon substrate using a 2D buffer layer is still a challenge.

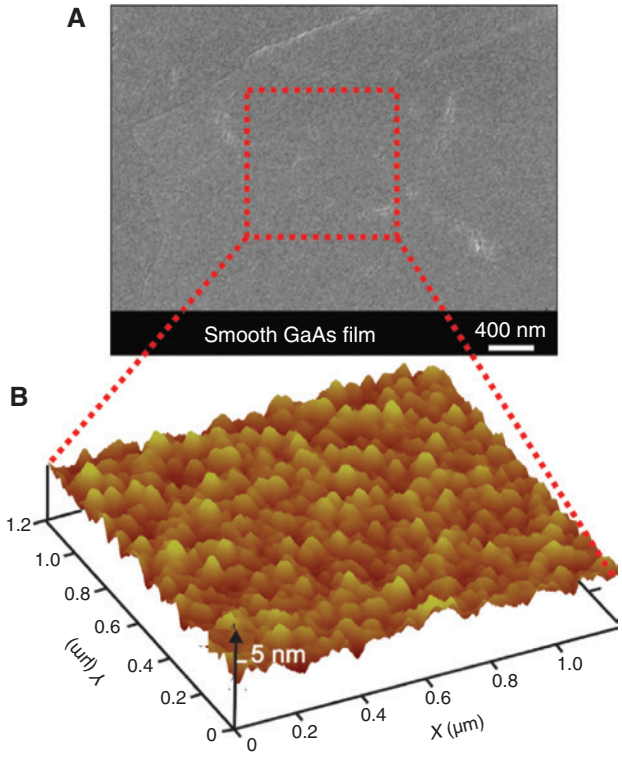

Figure 3: (A) SEM image of grown GaAs with Ga pregrown on multilayer graphene buffer layer. The surface shows smooth morphology, which is confirmed using (B) atomic force microscopy image. The measured root mean squared (RMS) roughness is around 0.6 nm with peak-to-peak value of 3 nm [6].

1.2 Organic photovoltaic

OPV is a type of solar cell that exploits organic semiconductors. Unlike conventional solar cells, OPVs can be produced with inexpensive, environmentally friendly, carbon-based materials. OPV's flexibility, transparency, lightweight nature, high absorption property, and the decent indoor performance are some of the key features that allow them to be integrated with portable electronic and biotronic devices [7].

Carbon-based molecular chains constitute the absorption layer or the active layer of the OPVs. These molecular polymers are deficient in delocalized charges when compared to inorganic counterparts. Hence, much less conductivity is notable in them [8]. However, specially prepared polymers can conversely provide delocalized electrons through the π bond system [8, 9]. As a famous example for polymers with delocalized electron encouraging bond arrangement, aromatic benzene molecule offers multiple π bonds that contribute to the conductivity enhancement in the material.

Specially prepared polymers can be put together to form a semi-*pn* junction with an internal electric field. This *pn* junction can be called acceptor/donor junction. The acceptor type of conductive polymers (analogues to p-type doped material) can take the form of a long molecular chain such as P3HT, while the donor type of "0D" carbon allotrope derivatives called fullerenes (analogues to n-type material) can take the form of PCBM. The donor/acceptor interface can be engineered to build various types of OPV devices.

The donor-acceptor interface can be realized either in a planar (PHJ) or bulk heterojunction (BHJ) configuration [10, 11]. The PHJ is considered the simplest structure of OPVs, which consists of sequentially deposited donor/acceptor layers through solution spin coating. The active layer is sandwiched between selective transport layers,

in addition to the contacts at both ends. Low efficiencies were observed with PHJs due to the extremely low nominal diffusion length for organic polymers, which is in the order of 10 nm, nearly five orders of magnitude less than silicon.

BHJ polymers, on the other hand, can be realized to supply more dispersed junction contour length, hence a higher probability for exciton to be dissociated. The method used to make a BHJ layer is to blend both the donor material and the acceptor material in an optimized ratio. Figure 4A shows the structure of both FPJ and BHJ OPV device, in addition to the typical band diagram of OPV.

OPVs have a total of four steps in order to collect a charge at the contacts. These four steps are (i) light absorption, (ii) exciton generation and diffusion, (iii) charge transport, and (iv) charge collection. The majority of organic semiconductors have high band gap values, which overwhelm the energy and the amount of absorbed photons. A great deal of research is taking place in terms of band-gap engineering to produce narrower band gaps.

In the pursuance of high-efficiency OPVs, research efforts have mainly focused on four critical directions. These directions include engineering new types of narrow-band-gap polymers; experimenting with different device

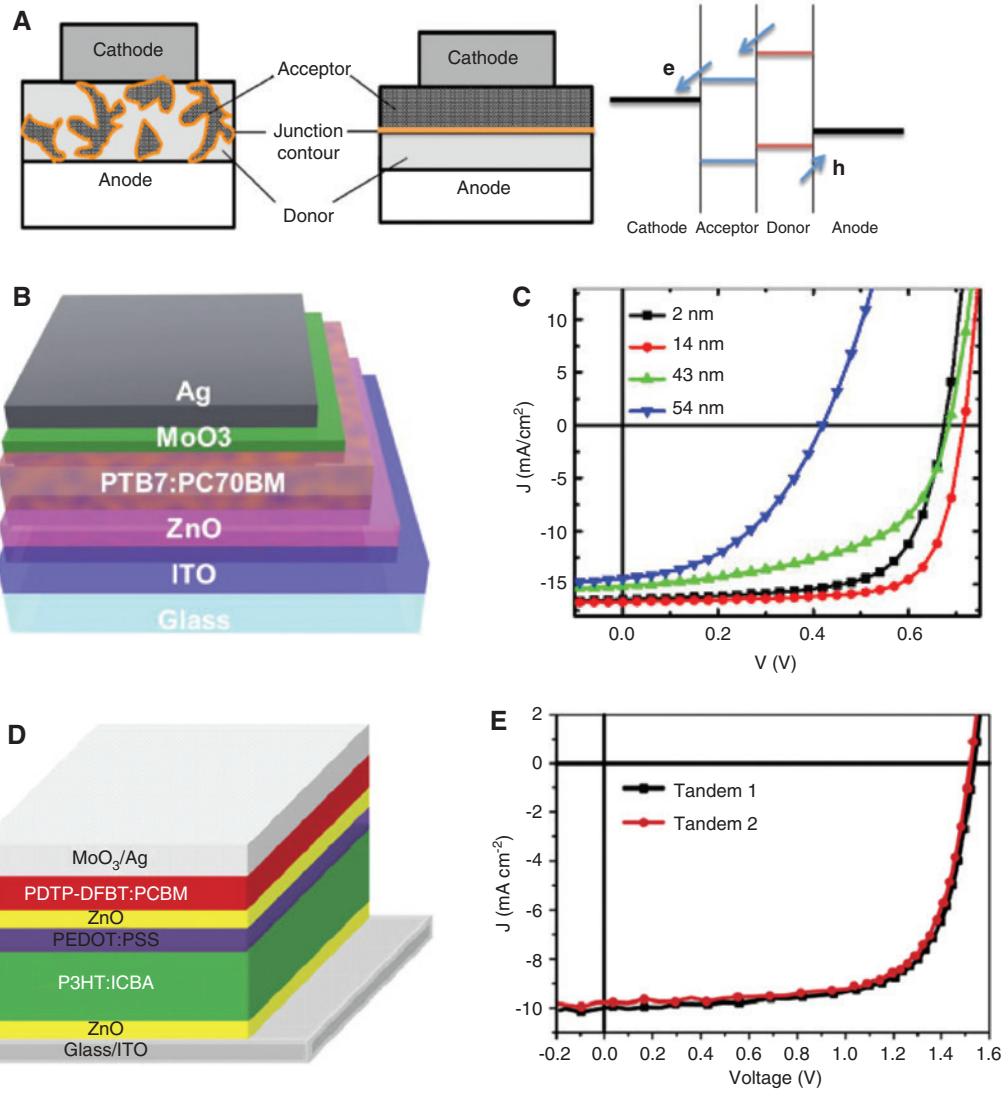

Figure 4: (A) BHJ structure (left), FPJ structure (middle), and typical band interfaces (right) of an OPV device. (B) Device schematic and (C) *J-V* curves at different ZnO layer thickness of the structure in (B) [12]. (D) Device structure and (E) measured *J-V* curves of the highest recorded efficiency of tandem organic solar cell [13].

structures in terms of tandem and buffer layer incorporation; light management techniques; and the incorporation of nanoparticles, nanotubes, or nanowires in different layers of the OPV structure.

The first direction was extensively studied in the last decade, and had significant impact in terms of breaking efficiency records [12–15]. Band-gap engineering in polymer materials has allowed the tuning of the interface levels of the polymers. Low-band-gap polymers are usually used as the donor materials and fullerene derivatives, such as PC71BM, have been widely adopted as the acceptor component given their relatively high electron affinity and charge carrier mobility. By definition, lower-band-gap materials will have higher catchment area of the solar spectrum, hence an increase in the internal quantum efficiency and consequently a boost to the short circuit current and power conversion efficiency. As an example, Figure 4B shows a recently studied OPV structure that employs a narrow-band-gap material [12]. The structure is created using an inverted OPV approach. The carrier selection layer was deposited using a low-temperature mist CVD method. In contrast to the high-temperature and low-vacuum traditional methods, this approach offers low-temperature and open-air pressure processing for depositing the ZnO selective layer. Avoiding high-temperature and high-vacuum processes are of a great importance to increase the economic feasibility, increase the process expediency, and protect the vulnerable organic layers from any damage and degradation, which could arise from high-temperature deposition. One of the advantages of using ZnO as a buffer layer is its selectivity in conducting electrons and blocking the holes in inverted structures. Additionally, ZnO offers higher electron mobility and light transparency.

Figure 4C shows the measured *J-V* characteristics at various buffer layer (ZnO in this case) thicknesses. According to the measured *J-V* curves, the best performance for such a cell occurs with ZnO thickness of 14 nm. The cell parameters at the optimal ZnO thickness are J_{SC}=16.6 mA/cm^2, V_{oc}=0.71 V, and *FF*=73%, with conversion efficiency of 8.6%.

It is worth mentioning that the current world efficiency record for single-layer OPV has been obtained very recently in 2016 by chemically modifying the solvent of the active polymers [16]. The work has made a simple approach, which is to replace the non-halogenated solvent with a hydrocarbon-based solvent, which also reduced the degradation of the active polymer itself. This high efficiency was reported by the same group that held the previous 11.5% world record OPV efficiency according to the latest National Renewable Energy Laboratory chart.

In terms of device structure innovation, tandem OPVs have offered a great utilization of covering a large range of the solar spectrum. You et al. have obtained the current world record that is held by this kind of structure [13]. As Figure 4D shows, the device structure incorporated two active layers with different effective band gaps, with an interlayer between them to aid common charge collection. The incorporation of two layers with different band gaps is to cover a wide range of the solar spectrum. At both ends (top and bottom), buffer layers were deposited to provide charge transport, finalized by an Ag contact from one side and a transparent ITO from the other. The *J-V* characteristics of the final structure are illustrated in Figure 4E. The obtained cell characteristics are J_{SC}=10.4 mA/cm^2, V_{oc}=1.4 V, *FF*=71%, and cell efficiency around 10.7%. The observed high V_{oc} value indicates that the two tandem layers are connected in series.

OPVs require careful examination of the contacts and the buffer layer work functions. The energy band alignment between the electrode of choice and the active layer polymer will significantly affect the charge collection (hence, the conversion efficiency). Failing to optimize the electrode/active layer interface will cause an accumulation of uncollected charges [17]. Aside from aligning the work functions and band edges, other techniques such as facilitating a buffer layer that blocks charges from going to the undesired electrode have been reported [18]. Moreover, degradation of the active layer could take place if the buffer layers as well as the contacts are not carefully chosen [19].

In terms of light management and optical properties, OPVs have witnessed many techniques to improve the efficiency. One example was the incorporation of metallic nanoparticles to use localized surface plasmon resonance (LSPR) [20]. LSPR is an optical phenomenon that takes place upon the interaction of metal nanoparticles with light. When the light wavelength is larger than the nanoparticle size, the LSPR commence. High oscillation of surface electrons forms a localized electric field around the nanoparticles, which, in turn, will increase the mobility. In addition to the mobility increase, the oscillation of electrons will emit light around the band-gap wavelength, which will increase the absorption, and ultimately the efficiency. LSPR can be tuned by many factors such as the material type, the geometrical size of the nanoparticles, the shape of the nanoparticles, and the spacing between these particles. Xue et al. have shown that the efficiency and fill factor have increased by 60% upon the incorporation of metallic nanoparticles [21]. Patterning of the buffer layer along with the antireflection coating layer is a

technique that has been used to boost photon harvesting [22, 23]. It did not, however, provide a landslide increase in the OPV metrics.

One of the key prospects for improving the open circuit voltage in OPVs is to reduce the density of trap states, which can be done by accurate control of the phase separated morphology, and by altering the interfacial arrangement of the donor/acceptor materials [24]. This approach of minimizing the interfacial trap states would help the fabrication of a thick photoactive layer, which, in turn, would increase the short circuit current without compromising the fill factor. Enhancing the contact work function alignment by accurate choice of materials, in conjunction with reducing the width of the Gaussian density of state, is one of the encouraging routes for enhancing the V_{oc}.

2 Optoelectronics using carbonaceous materials

2.1 Graphene-based devices

The atomically thin graphene layer exhibits extraordinary electrical and optical properties. Some of these properties include high electron mobility [25], high mechanical strength with Young's modulus of 1 TPa [26], and high thermal conductivity [27]. Yet, graphene is not applicable for most of the semiconductor applications due to the absence of the band gap. It is only possible to open a band gap in bilayer graphene by applying a vertical electric field [28], which poses a major constraint for fabricating large-scale electronics based on graphene devices.

Graphene optoelectronics, however, have been extensively studied. Fundamentally, monolayer graphene is relatively transparent between visible to infrared [29, 30]. It can be grown using CVD [31]. Recently, Kim et al. have shown bright light emission from a suspended graphene flake [32], proving that graphene can be used as a light emitter. Nevertheless, due to the semimetal nature of graphene, photodetectors based on graphene do not show a photovoltaic effect, which is the essential mechanism in current conduction in solar cells. Instead, they show a photo-thermoelectric effect where a temperature gradient is created optically, forcing the generated carriers to move from the hotter side to the colder side [33]. There have been extensive studies on graphene photodetectors. Here, we will focus on graphene/silicon junction, which can be easily scaled for commercialization.

Graphene/silicon junction is a promising device structure for large-scale optoelectronic applications. Graphene/silicon junction is fundamentally a Schottky junction, which can be useful for various energy-harvesting applications, including low-energy optical switches when used as photodetectors. Several groups have investigated the optical and the electrical properties of this structure [34–39]. Figure 5A shows a typical graphene/silicon device where the graphene is in contact with the silicon substrate (in this case, n-type silicon substrate). The gold electrodes can be modified according to the preference of the group, as in the case of Figure 5B, where the measurements were taken with silver paste and gallium-indium eutectic electrodes as top and bottom contacts, respectively. In this figure, the current density-voltage characteristics are illustrated for the graphene/silicon device when operated as a solar cell and at different stages of treatment [40]. The black curve illustrates the solar cell *J-V* curve for a bare graphene/silicon junction. The observed efficiency is 3.78% with J_{SC}=22.9 mA/cm^2 and V_{oc}=0.387 V. These parameters can be enhanced by various methods. The first method is doping the graphene, which is illustrated as the red curve in Figure 5B. The purpose of doping in this structure is to enhance the open-circuit voltage as well as the fill factor. Consequently, the observed efficiency after HNO_3 doping is 8.91% with J_{SC}=23.89 mA/cm^2 and V_{oc}=0.548 V. The yellow curve in the figure corresponds to the doped graphene/silicon junction after coating with TiO_2 layer. Such a layer acts as an antireflection layer, minimizing the reflected incident light. For this particular cell, the performance parameters measured are V_{oc}=0.60 V, J_{SC}=32.5 mA/cm^2, *FF*=73%, and efficiency of 14.1%.

The stability of the graphene/silicon junction solar cell after treatment is a major issue. In Figure 5C, the cell characteristics are measured on different days. The cell characteristics degraded after 20 days. This degradation occurred due to the instability of the doping technique used to dope the graphene flake. In fact, the cell efficiency is slightly enhanced after re-doping the graphene flake with HNO_3, giving 14.5% efficiency. To our knowledge, this efficiency obtained represents the highest efficiency reported to date on graphene/silicon structure. Yet, the stability of this structure to maintain this high efficiency is a subject of research.

The graphene/silicon junction can also be used as a photodetector [36]. In Figure 5D, the current-voltage characteristics of the device are illustrated at various incident optical powers. As shown, the maximum observed photocurrent occurs when the device is reverse biased, where the excited carriers are injected from the silicon to the graphene flake. This is because in the reverse biased condition, the

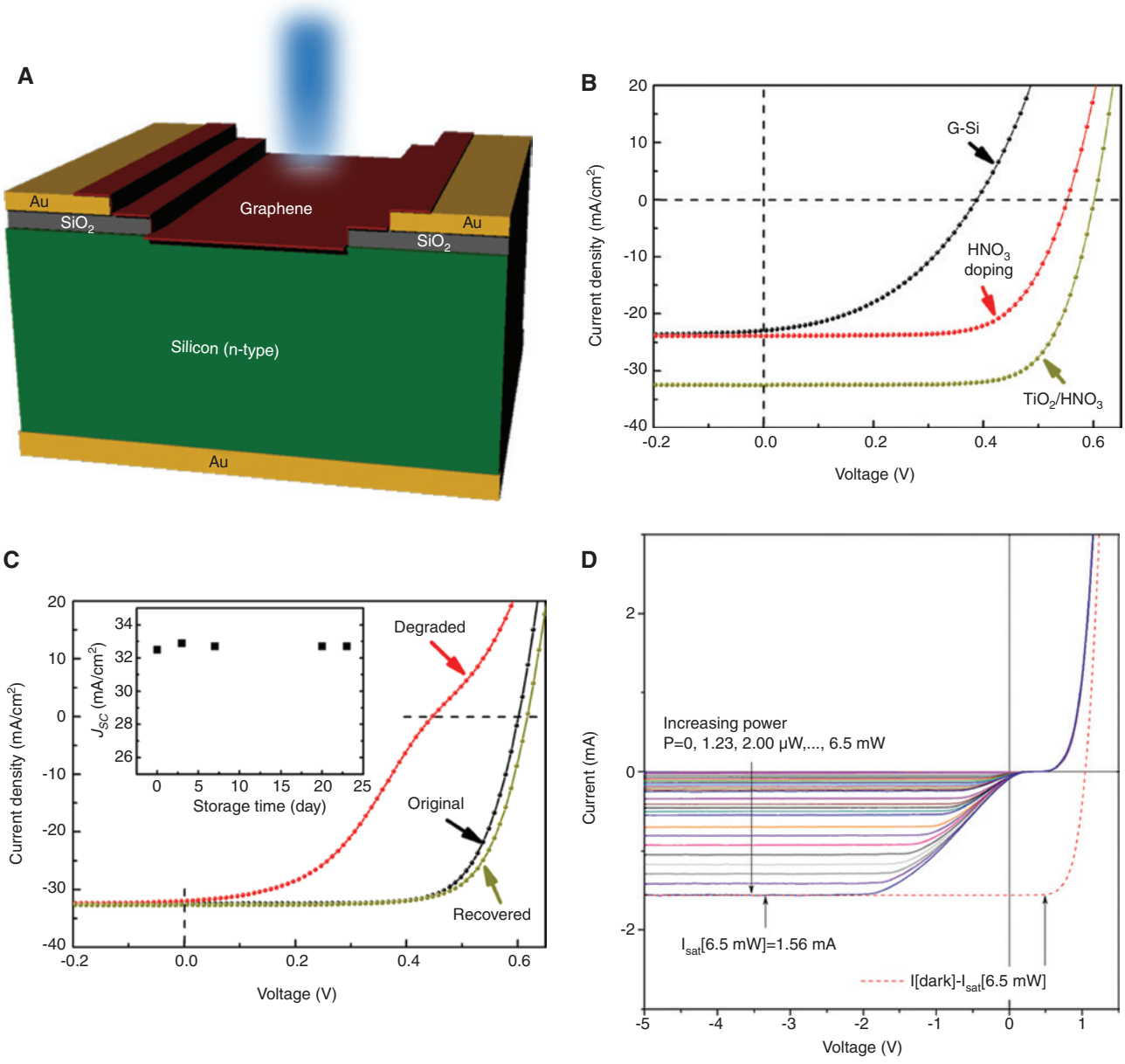

Figure 5: (A) Schematic diagram of the graphene/silicon device. (B) Measured *I-V* curves of the graphene/silicon device when used as a solar cell. The black curve is the solar *I-V* of bare graphene on silicon. The red curve is after doping the graphene with HNO_3, and the yellow curve is the solar *I-V* after spin coating with TiO_2 [40]. (C) Solar *I-V* curves of the device in (B) showing the degradation of the cell performance after a long period of time. The recovered curve is measured after doping the cell with HNO_3. The inset shows the short-circuit current as a function of time. (D) Measured *I-V* curves of the graphene/silicon device at several incident laser powers when used as a photodetector [36].

difference in the Fermi level opens large numbers of available states, allowing large numbers of photoexcited carriers [36]. For this structure, the reported incident photon conversion efficiencies can be as high as 57% and the maximum responsivity is 435 mA/W. This high efficiency along with the high responsivity illustrates the potential use of graphene/silicon devices for photodetection applications.

We believe the obtained efficiency for this type of graphene devices can be optimized by various techniques. First, the existence of the native oxide between the graphene flake and the silicon substrate can degrade the device performance [35]. This layer could either be grown during the transfer of graphene or even after the graphene deposition. Such an issue can be prevented by careful fabrication techniques and considering different passivation layers. Another method to increase the efficiency is doping the graphene *p*-type (for n-type Si substrate). This will shift the Fermi energy in the graphene region to the

valence band, making it easy to bias the device, hence low-power operations with high conversion efficiency. However, the doping method, doping concentration characterization, device stability with time, and doping-to-defect ratio are some of the crucial key points that need to be carefully addressed.

2.2 Carbon nanotube-based devices

Carbon nanotube research in the last few years have witnessed major improvements in terms of solving the grand challenges of carbon nanotube synthesis, which include purity and chirality control. Solving the synthesis issue will substantially put carbon nanotube electronic and optoelectronic devices on the industrial roadmap. A recent study to fabricate thin film transistors with high-purity semiconducting nanotubes has shown a large I_{on}/I_{off} ratio with large turn-on current using ultra-high-purity semiconducting carbon nanotubes. The high-purity semiconducting nanotube solution has enabled the realization of large-scale integration of nanotubes for electronics applications [41]. The potential of using carbon nanotube devices for electronic applications can be realized in the near future.

In an attempt to control the nanotube's chirality, Liu et al. have used a carbon nanotube seed to "clone" the same chirality by optimizing the CVD growth parameters [42]. The resulting elongated nanotube exhibited the exact chirality as the starting seed. The method highlights the first attempt to produce a specific chirality nanotube, which depends on the starting seed. Yet, the challenge of scaling this method to industrial applications has been hinged on the full control of the placement of the cloned nanotubes in the desired positions. Some proposed solutions include nanotube transfer from one substrate to another. However, this approach can induce defects and possible degradation of the nanotube's performance.

Although all these attempts to solve the synthesis issues for large-scale integration are still under investigation, the optoelectronic properties of carbon nanotubes have been extensively studied in the past few years [43–48].

Nanotubes have a direct band gap, which do not require any phonons to emit or absorb a photon. They exhibit strong exciton binding energy due to the 1D nature of these materials. In terms of applications, these excitonic transitions can be used for various biomedical sensing and communication applications [49, 50]. When biased in a *pn* junction configuration, semiconducting nanotubes exhibit ideal diode behavior [51], efficient photocurrent detection [52], and photocurrent enhancement at the excitonic transitions.

Recent studies on carbon nanotube/silicon junction, similar to the graphene structure in Figure 6A, have shown high conversion efficiencies [53, 55]. Unlike the graphene/silicon junction, semiconducting carbon nanotube/silicon junction is ideally a *pn* junction. However, due to uncontrollable CVD growth process, a mixture of metallic and semiconducting nanotubes are produced, rendering a Schottky junction with the underlying silicon substrate. Figure 6A illustrates the device structure where the nanotube thin film is lying on top of the silicon substrate. In Figure 6B, the solar cell *J-V* characteristics of CVD-grown nanotubes on n-type silicon substrate are demonstrated. The measurements were taken under non-concentrated AM 1.5 analogues to Figure 5B; the device is coated with TiO_2 antireflection coating layer and chemically doped using HNO_3. The resulting solar cell characteristics, after applying the treatment processes, are V_{oc}=0.61 V, J_{SC}=32 mA/cm^2, *FF*=77%, and efficiency of 15%, which is quite high for such a device. Nevertheless, the carbon nanotube/silicon junction suffers from time stability, similar to the graphene/silicon junction, due to doping degradation, which can be resolved by chemically doping the cell with HNO_3.

It should be noted that semiconducting nanotubes suffer from a large contact resistance. In fact, research is still undergoing to optimize the contact resistance of carbon nanotubes [56, 57]. The current findings suggest that nanotubes with diameters between 1.5 and 1.6 nm start to collapse under the deposited metal and affect the device performance.

Quasi-metallic nanotubes, on the other hand, are surfacing to become useful for optoelectronic applications. Ideally, metallic nanotubes do not exhibit a band gap [58], mainly due to the absence of this band gap whenever quasi-metallic nanotubes are lying on a substrate [59]. One of the advantages quasi-metallic nanotubes exhibit is low contact resistance due to the absence of Schottky contacts, as opposed to their semiconducting counterparts. They also exhibit higher photocurrent values compared to semiconducting nanotubes [60]. Figure 6C shows a suspended quasi-metallic carbon nanotube *pn* device. The split gate in the bottom of the trench can be biased separately to induce electrostatic doping. In Figure 6D, we showed photocurrent enhancement of this carbon nanotube photodetector with increasing electrostatic doping [54]. The obtained efficiency was <1%.

The peak in Figure 6D corresponds to the excitonic transition E^{11} of the nanotube. In fact, a recent study showed that quasi-metallic nanotubes can exhibit photo-thermoelectric effect, similar to graphene

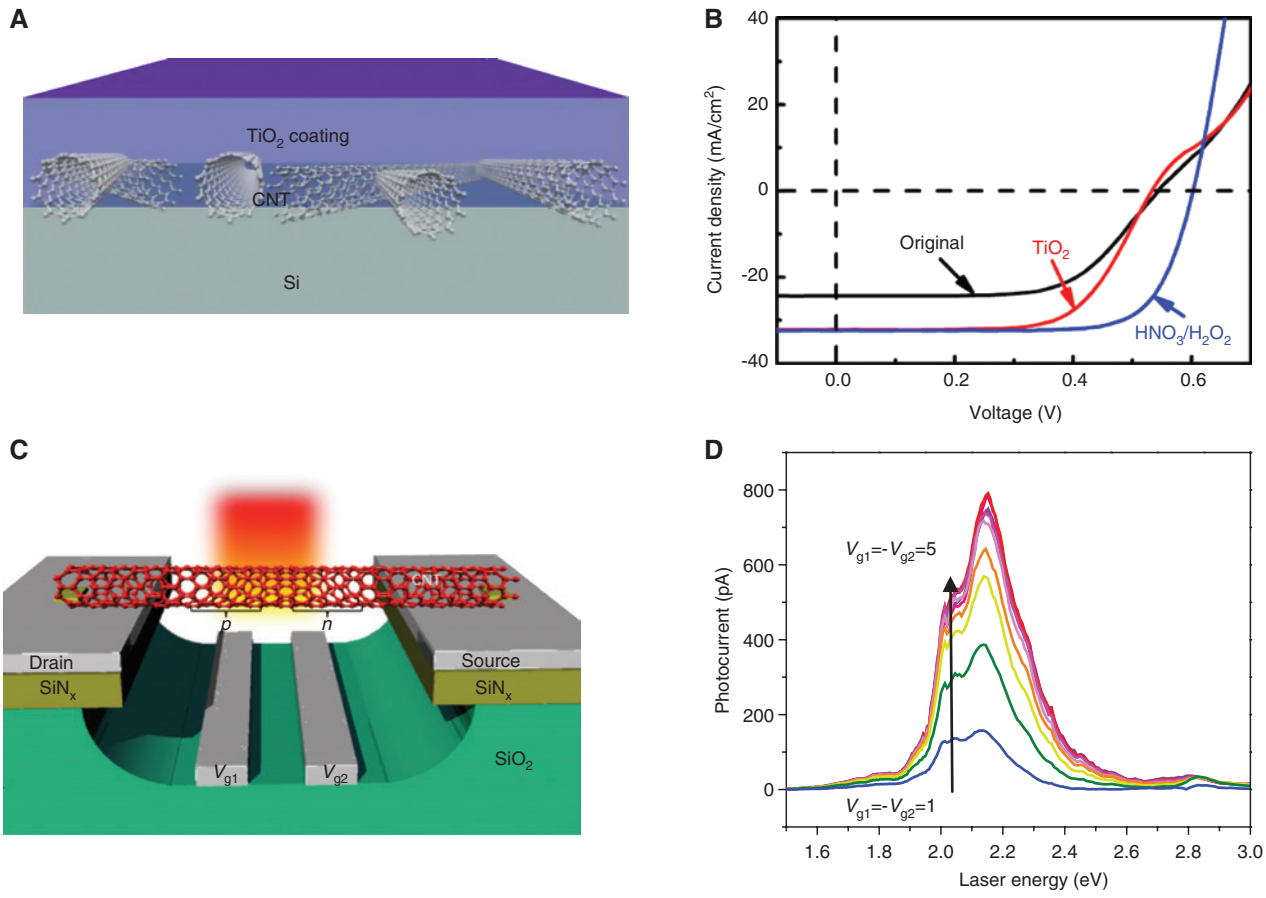

Figure 6: (A) Schematic diagram of the carbon nanotube/silicon junction with TiO_2 layer as an antireflection coating layer. (B) The measured *J-V* of the structure in (A) at different treatment processes. The highest efficiency obtained after HNO_3/H_2O_2 doping and TiO_2 coating [53]. (C) Schematic diagram of carbon nanotube photodetector using a split gate structure. (D) Photocurrent enhancement with increasing gate voltage (V_{g1}=-V_{g2}) for the structure in (C) [54].

photodetectors, if the mini-gap is less than the exciton binding energy (50 meV in this case) [61]. For band gaps >50 meV, the photovoltaic effect dominates the photocurrent transport. Although the efficiency of this photodetector is <1%, this work was the first demonstration of quasi-metallic nanotubes as photodetectors. Thanks to the mini-gap that metallic carbon nanotubes exhibit, optoelectronics based on quasi-metallic nanotube devices can be realized.

3 Challenges and opportunities for low-dimensional materials

3.1 Photovoltaic devices

The possibility of implementing nanodevices for energy-generation applications is rapidly increasing. Many of the unknown fundamental physical and chemical properties are being discovered on a daily basis. Advancements in material fabrications have led to new emerging devices based on 2D materials. The most prominent 2D materials to date are molybdenum disulfide (MoS_2), tungsten diselenide (WSe_2), tungsten sulfide (WS_2), and phosphorene. Experimental investigations using these devices show that photovoltaic devices can be easily scaled down to the nanosize without complex fabrication processes. For example, Buscema et al. have shown that black phosphorus multilayers exhibit a photovoltaic effect when an electrostatic homojunction is created [62], analogous to the nanotube in Figure 6C. Other similar studies on MoS_2 and WSe_2 show similar effects [63, 64]. We should mention that devices based on the split gate structure are ideal for understanding the physical phenomena associated with the material under study. Nonetheless, electrostatic doping requires two separate electrodes, hence two voltage sources, which render the device inefficient

and impractical for industrial applications. A more scalable design is required to achieve similar or even better performance.

Tsai et al. measured the solar cell performance of MoS_2/silicon junction. The results yielded V_{ov}=0.41 V, J_{sc}=22.36 mA/cm^2, *FF*=57.26%, with efficiency of 5.23% [65]. Although these cell characteristics are lower than those of graphene/silicon junction, it was the first demonstration of MoS_2/silicon junction solar cell, which can be further improved by several treatments, similar to the graphene/silicon junction discussed above.

Another interesting photovoltaic approach is van Der Waals stacking of 2D materials to create *pn* junctions. Many groups have investigated this approach with different 2D layers [64, 66–68]. The maximum reported external quantum efficiency, to our knowledge, is 34% for multilayer MoS_2/WSe_2 *pn* junction [67]. In fact, Furchi et al. measured the solar cell response of monolayer MoS_2/WSe_2 *pn* junction and found a conversion efficiency <1% [69]. Similar conversion efficiency has been obtained using GaTe-MoS2 *pn* junctions. Although 2D stacked structures exhibit high quantum efficiency, the solar cell behavior of such structures requires adequate improvements in order to achieve low-cost 2D solar cells.

As discussed in Section 1, the tandem cell approach is very promising given less fabrication processes (and hence cost effectiveness). In Figure 7A, the solar spectrum is illustrated. Most of the low-dimensional photovoltaic devices we mentioned in this article fall in the visible to mid-infrared regime (approximately between 500 and 1200 nm). Although integrating some III-V semiconductors can cover the entire spectrum, there are still wide solar spectrum regions that need to be investigated using 2D materials, especially in the infrared. In fact, carbon nanotubes and graphene have been used as infrared detectors [70–72]. The detection mechanism of these carbonaceous devices is mainly bolometric. They also suffer from low conversion efficiency. Another candidate for infrared detection studies is black phosphorus, where the band gap is around 0.3 eV [73]. To this date, no reported studies have been published due to the recent discovery of this 2D layer.

3.2 Thermoelectric devices

So far, we have discussed photovoltaic devices that operate by converting the incident photons to electricity. Another source of energy that solar power provides is heat. Some geographic areas exhibit high temperatures, especially during the summer. This wasted heat can be a good source of energy if invested wisely. Thermoelectric devices are one way to use this wasted heat. Figure 7B shows a schematic diagram of a thermoelectric power generator. The Seebeck phenomenon, which is the sole mechanism of thermoelectric devices, arises when the surface of a material is thermally excited. This leads to a temperature gradient across the material. During the process, carriers tend to move from the hot side to the cold side. For an n-type (p-type) material, electrons (holes) will move from the top to the bottom, creating an electric current. For a thermoelectric generator to work, three main features are required: a heat source, a heat sink, and a thermoelectric material.

Unfortunately, current thermoelectric devices are poorly used for power-generation applications. Reasons such as low heat-to-electricity conversion, toxicity, and expensive materials are some of the major obstacles that face thermoelectric devices [74–76]. The most common material used for thermoelectric devices is bulk bismuth telluride Bi_2Te_3 and its alloys. Materials based on Bi_2Te_3 have thermoelectric figure of merit (*ZT*) values ranging between 0.5 and 1 [76, 77]. Thermoelectric generators based on Bi_2Te_3 suffer from low conversion efficiency and complex fabrication techniques. Nevertheless, researchers have been trying to fabricate materials with $ZT>1$ [78]. In principle, this is a challenging task since $ZT=S^2\sigma T/\kappa$, where S is the Seebeck coefficient, σ is the electrical conductivity, T is the absolute temperature, and κ is the thermal conductivity. It is essential to have high electrical conductivity with low thermal conductivity, in order to have high *ZT*. However, it is quite an obstacle to obtain materials with these specifications.

At the nanoscale, due to low dimensionality, which causes the confinement of the lattice temperature (heat), it is predicted that material thermal properties should be substantially enhanced [76, 79]. For instance, black phosphorus and phosphorene (monolayer black phosphorus) exhibit low thermal conductivity with high electrical conductivity in the armchair direction, which are two important thermoelectric properties that are hard to find. Black phosphorus has thermopower (*S*) as high as 2000 μV/k for monolayer, with thermal conductivity as low as 18 (W/m-K), and electrical conductivity in the order of 10^3 S/m [80, 81]. Using these parameters, several studies have found that black phosphorus exhibit a thermoelectric figure of merit (*ZT*) ranging between 1 and 2.5 for monolayers [81, 82]. In fact, due to its recent discovery, and according to a recent study on the electron transport of phosphorene, it was found that the thermoelectric properties can be dramatically degraded if the electron-phonon coupling effect was not taken into account. The

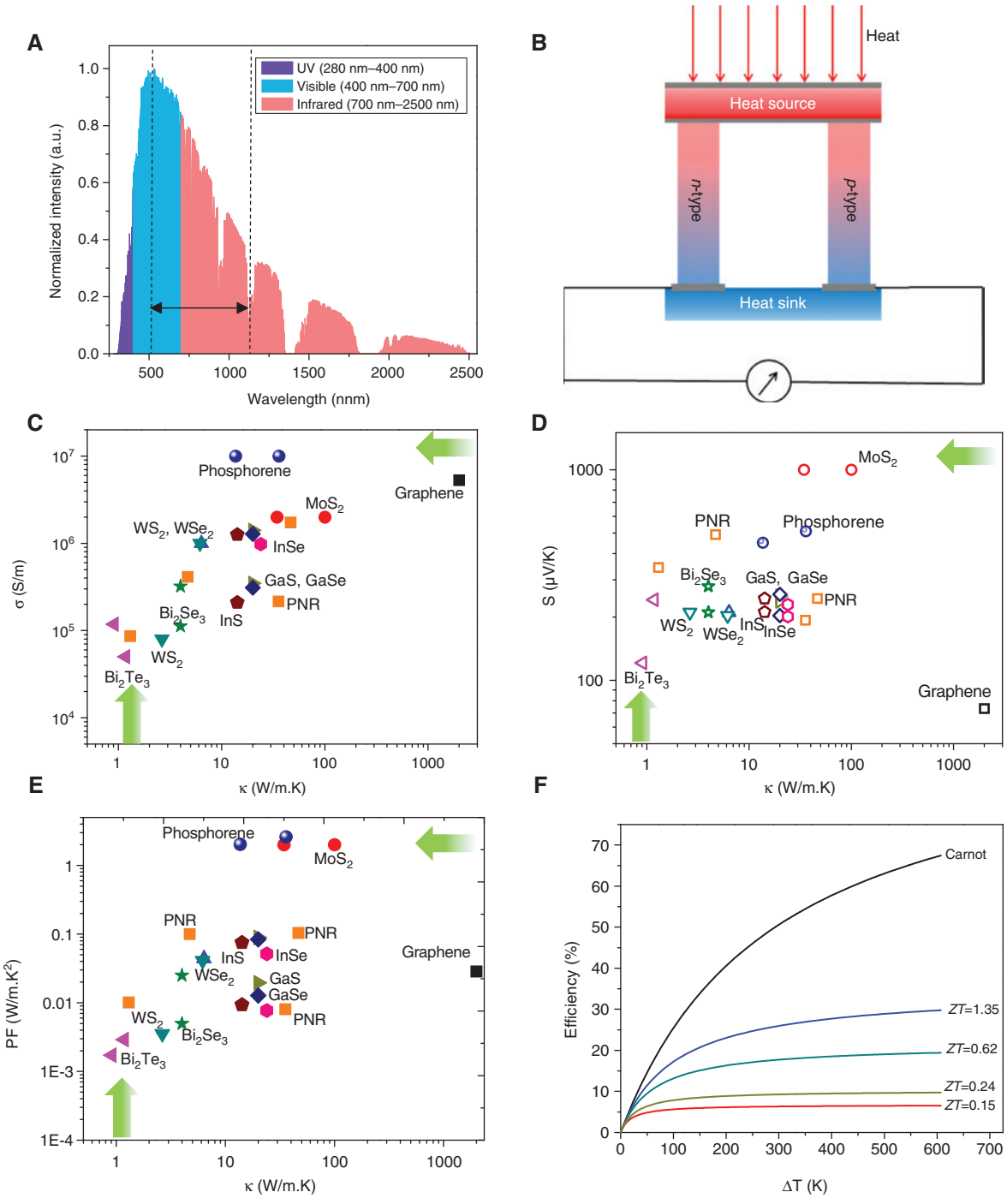

Figure 7: (A) Solar spectrum vs. wavelength. The region between the dashed lines is where most low-dimensional devices discussed in this article can cover. (B) Schematic illustration of the thermoelectric power generator. The contrast in the temperature between the top and the bottom of the thermoelectric material results in current generation, which is detected by the external resistor. (C) Electrical conductivity, (D) Seebeck coefficient, and (E) power factor at different thermal conductivities for several 2D materials obtained from the literature. The arrows indicate the desired area where a good thermoelectric materials should fall in. (F) Estimated conversion efficiency of some of the 2D materials discussed in Table 1. For an ideal thermoelectric device, the maximum attained efficiency should reach the Carnot efficiency (black curve).

modified *ZT* drops to 0.15 at room temperature [83]. Thus, we believe concrete and reliable experimental studies on the fundamental thermoelectric properties of phosphorene and black phosphorus are crucial.

Another recently investigated 2D material is MoS_2. Buscema et al. measured the Seebeck coefficient of monolayer MoS_2, and found it to fall in the range between 4×10^2 and 1×10^5 [84], which is significantly larger than that of

bulk MoS_2. This large Seebeck coefficient can be tuned by applying a vertical electric field across the flake, as in the case of gate voltage. Yan et al. also measured the thermal conductivity of monolayer MoS_2 using the Raman spectroscopy technique [85]. The obtained thermal conductivity value was 34 (W/m-K). This value is much less than the simulated values by approximately twofold. Accordingly, the thermoelectric figure of merit of monolayers MoS_2 ranges between 0.24 and 1.3. We should mention that calculated *ZT* values assume ballistic transport while neglecting the various scattering mechanisms in each material.

In Table 1, we summarize the properties of several 2D materials. We should note that there is significant discrepancy between the values reported for the thermoelectric properties of each material. Most of the values in the table are based on calculations instead of experimental measurements, where certain assumptions are made (i.e. ballistic electron transport). This can be a major source of error in obtaining the actual thermoelectric properties. Moreover, thermoelectric calculations ignore the doping technique, which renders the calculated *ZT* values unrealistic if the doping cannot be realized. Lastly, the contact resistance at the thermoelectric material-electrode interface is ignored, which imposes another barrier to overcome in order to obtain high heat-to-electricity conversion efficiency.

In Figure 7C and D, we plot the electrical conductivity vs. thermal conductivity and the thermopower vs. thermal conductivity using values obtained from literature, respectively. We also plot the power factor ($PF=S^2\sigma$) in Figure 7E.

Table 1: Thermoelectric properties of several 2D materials.

Material/property	Lattice constant (Å)	Band gap (eV)	Electrical conductivity σ (S/m)		Thermal conductivity K_{th} (W/m-K)	Seebeck coefficient *S* (μV/K)	*ZT* at 300 K
MoS_2		1.9 [86][a]			17.78 [87]	200 [87]	1.35 [87]
	3.12	1.6 [87]	2E+ [87]		0.6 [88]	200 [88]	0.24 [88]
	3.179 [87]	1.75 [88]	1.2E+4 [88]		100 [89]	1500 [84][a]	0.53 [88]
		1.7 [88]			34.5 [85][a]	220 [88]	0.65 [88]
						200 [84]	
WSe_2		1.254 [87]			6.38 [87]	200 [87]	1.88 [87]
	3.319 [87]	1.2 [88]	1E+6 [87]		0.4 [88]	210 [88]	0.35 [88]
		1.7 [88]	1.2E+4 [88]			210 [88]	1.2 [88]
WS_2	3.183 [87]	1.573 [87]	1E+6 [87]		2.646 [88]	203 [87]	2 [87]
			8E+4 [88]		6.18 [87]	210 [88]	0.4 [88]
Bi_2Te_3		0.105 [90]	5E+4 [91][a]		1.75 [92][a]	247 [92][a]	0.62 [91][a]
	4.3856 [91]	0.15 [94][a]	11.8E+4 [93][a]		1.18 [91][a]	241 [91][a]	0.56 [93][a]
					0.91 [93][a]	121 [93][a]	
GaS [95]	3.630	2.563	$1.41E+6_{p\text{-type}}$		$20_{p\text{-type}}$	$251.6_{p\text{-type}}$	$1.42_{p\text{-type}}$
			$3.48E+5_{n\text{-type}}$		$20_{n\text{-type}}$	$237.0_{n\text{-type}}$	$0.62_{n\text{-type}}$
GaSe [95]	3.755	2.145	$1.28E+6_{p\text{-type}}$		$20_{p\text{-type}}$	$256.1_{p\text{-type}}$	$1.07_{p\text{-type}}$
			$3.10E+5_{n\text{-type}}$		$20_{n\text{-type}}$	$202.9_{n\text{-type}}$	$0.172_{n\text{-type}}$
InS [95]	3.818	2.104	$1.26E+6_{p\text{-type}}$		$14.2_{p\text{- type}}$	$244.2_{p\text{-type}}$	$1.38_{p\text{-type}}$
			$2.10E+5_{n\text{-type}}$		$14.2_{n\text{- type}}$	$210.8_{n\text{-type}}$	$0.191_{n\text{-type}}$
InSe [95]	4.028	1.618	$9.81E+5_{p\text{-type}}$		$24_{p\text{-type}}$	$229_{p\text{-type}}$	$0.592_{p\text{-type}}$
			$1.92+5_{n\text{-type}}$		$24_{n\text{-type}}$	$200.5_{n\text{-type}}$	$0.092_{n\text{-type}}$
Bi_2Se_3 [95]	4.140	0.5103	$3.21E+5_{p\text{-type}}$		$4_{p\text{-type}}$	$279.3_{p\text{-type}}$	$0.1.76_{p\text{-type}}$
			$1.12E+5_{n\text{-type}}$		$4_{n\text{-type}}$	$210.1_{n\text{-type}}$	$0.249_{n\text{-type}}$
Graphene [95]	2.461	0–0.2 [28]	5.3E+6		2000	73.4	0.0108
Phosphorene	(zigzag)	2 [83]	p-type	10 E+6 [97]	36 [98]	510 [83]	0.15 [83]
	3.3	1.5 [96]					1.3 [81]
	(Armchair)	1.51 [99]	n-type		13.65 [96]	450 [83]	0.1 [83]
	4.53						1.3 [81]
	[100]						
Phosphorene	4.53 [100]	0.6 [99]	p-type [99]	8.6E+4 [99]	1.3 [99]	343.1 [99]	2.3 [99]
nanoribbon (armchair)			n-type [99]	4.13E+5 [99]	4.70 [99]	-492. [99]	6.4 [99]
Phosphorene	3.3		p-type	17.4E+5 [99]	46.66 [99]	244.2 [99]	0.7 [99]
nanoribbon (zigzag)	[100]	1.6	n-type	2.16E+5 [99]	35.48 [99]	-193.2 [99]	0.1 [99]

The reported values with [a]are obtained from experiments.

The arrows in these figures indicate the desired direction for an ideal thermoelectric material. Accordingly, phosphorene (armchair) and MoS_2 exhibit high thermoelectric properties, compared to Bi_2Te_3, although the thermal conductivity of Bi_2Te_3 is one of the lowest compared to other materials. While graphene exhibit one of the highest electrical conductivities, it suffers from very high thermal conductivity, which renders graphene thermoelectric devices impractical. Other 2D materials plotted in the figures also exhibit noticeably good thermoelectric properties. Thus, we believe 2D materials, such as phosphorene and MoS_2, can be potential candidates for thermoelectric device applications.

To this end, we can estimate the thermoelectric efficiency based on some of the reported *ZT* values in Table 1. The simplified efficiency is given by [75, 101]

$$\eta=\frac{\Delta T}{T_{\text{hot}}}\frac{\sqrt{1+ZT}-1}{\sqrt{1+ZT}+\frac{T_{\text{cold}}}{T_{\text{hot}}}},$$

where η is the device efficiency; T_{hot} and T_{cold} are the hot and cold temperatures at both ends of the material, respectively; and ΔT is the difference between T_{hot} and T_{cold}. In Figure 7F, we plot the estimated efficiencies for some of phosphorene and MoS_2 reported *ZT* values. Of course, the plotted curves are estimates only and assume constant *ZT* across the calculated temperature range, which can be a source of error in finding the actual efficiencies [102]. It is worth mentioning that to obtain high *ZT* values for monolayer flakes, robust studies on the doping concentration should be investigated. One common doping method is electrostatic gating, as in the case of Figure 6C; however, this method requires a voltage source, which is not efficient for energy-generation applications. Chemical doping to obtain high *ZT*, however, is still another room of research.

4 Concluding remarks

In conclusion, we have discussed some recent nanodevices that can offer promising alternatives for clean and sustainable energy generation. Integration of III-V semiconductors on silicon has shown significant progress in recent years. III-V nanowires on silicon and using 2D buffer layers between III-V semiconductor and silicon substrate have shown relatively lattice match conditions, hence good routes toward efficient solar cells. Moreover, recent OPVs, which hold big promise for thin and flexible optoelectronics, have been highlighted. Although the efficiency of these cells is still low, there is a large room for improvement using this type of solar cells.

We also discussed recent devices using carbonaceous devices. Graphene/silicon junctions are one approach for scalable electronics, especially with recent advances in graphene synthesis. Carbon nanotubes, on the other hand, exhibit extraordinary optical properties; however, they still lack concrete fabrication and synthesis techniques for scalable optoelectronic applications.

Along with carbonaceous materials, we discussed new emerging devices, such as MoS_2 and WSe_2. Although they have been recently discovered, researchers have shown quantum efficiencies as high as 34% for MoS_2/WSe_2 multilayer, only by flake stacking, while the photon to energy conversion obtained for the monolayer structure is <1%. Such a route to fabricate scalable optoelectronic devices requires more investigations in order to unlock doors for nano-optoelectronics in clean and sustainable energy generation.

We finally show that thermoelectric devices based on 2D materials can compete with state-of-the-art bismuth telluride and its alloys. In particular, phosphorene and MoS_2 hold great promise as candidates for thermoelectric devices. However, a proper doping technique in order to provide the expected thermoelectric performance is still lacking.

Still, the gap between industrial implementation and academic research is noticeably significant, although scientists and engineers have shown great scientific progress in discovering many of the fundamental properties surrounding 1D and 2D materials. Indeed, the shift from laboratory experiments to large-scale production of nanodevices is faced with fabrication and design issues. Optimized functional nanodevices for clean and sustainable energy generation is still a challenge we look forward to overcome.

Acknowledgments: The author would like to acknowledge support from KACST through the Center of Excellence for Green Nanotechnologies, part of Joint Centers of Excellence Program.

References

[1] Koppes M, Hallet B, Rignot E, Mouginot J, Wellner JS, Boldt K. Observed latitudinal variations in erosion as a function of glacier dynamics. *Nature* 2015, 526, 100–103.

[2] Hallegatte S, Bangalore M, Bonzanigo L, Fay M, Kane T, Narloch U, Rozenberg J, Treguer D, Vogt-Schilb A. *Shock Waves: Managing the Impacts of Climate Change on Poverty*, World Bank Publications: Washington, DC, 2015.

[3] Green MA, Emery K, Hishikawa Y, Warta W, Dunlop ED. Solar cell efficiency tables (version 47). *Prog. Photovolt. Res. Appl.* 2015, 23, 805–812.
[4] Press Release. Fraunhofer Institute for Solar Energy Systems (www.ise.fraunhofer.de/en/press-and-media/press-releases/press-releases-2014/new-world-record-for-solar-cell-efficiency-at-46-percent), 1 December, 2014.
[5] Yao M, Cong S, Arab S, Huang N, Povinelli ML, Cronin SB, Dapkus PD, Zhou C. Tandem solar cells using GaAs nanowires on Si: design, fabrication, and observation of voltage addition. *Nano Lett.* 2015, 15, 7217–7224.
[6] Alaskar Y, Arafin S, Wickramaratne D, Zurbuchen MA, He L, McKay J, Lin Q, Goorsky MS, Lake RK, Wang KL. Towards van der Waals epitaxial growth of GaAs on Si using a graphene buffer layer. *Adv. Funct. Mater.* 2014, 24, 6629–6638.
[7] Li G, Zhu R, Yang Y. Polymer solar cells. *Nat. Photon.* 2012, 6, 153–161.
[8] Cuniberti G, Fagas G, Richter K. *Introducing Molecular Electronics: A Brief Overview*. Springer: Berlin, 2006.
[9] Faraday M. On new compounds of carbon and hydrogen, and on certain other products obtained during the decomposition of oil by heat. *Philos. Trans. Roy. Soc. Lond.* 1825, 115, 440–466.
[10] Glenis S, Horowitz G, Tourillon G, Garnier F. Electrochemically grown polythiophene and poly (3-methylthiophene) organic photovoltaic cells. *Thin Solid Films* 1984, 111, 93–103.
[11] Yu G, Gao J, Hummelen JC, Wudl F, Heeger AJ. Polymer photovoltaic cells: enhanced efficiencies via a network of internal donor-acceptor heterojunctions. *Science* 1995, 270, 1789.
[12] Zhu X, Kawaharamura T, Stieg AZ, Biswas C, Li L, Ma Z, Zurbuchen MA, Pei Q, Wang KL. Atmospheric and aqueous deposition of polycrystalline metal oxides using mist-CVD for highly efficient inverted polymer solar cells. *Nano Lett.* 2015, 15, 4948–4954.
[13] You J, Dou L, Yoshimura K, Kato T, Ohya K, Moriarty T, Emery K, Chen CC, Gao J, Li G. A polymer tandem solar cell with 10.6% power conversion efficiency. *Nat. Commun.* 2013, 4, 1446.
[14] He Y, Li Y. Fullerene derivative acceptors for high performance polymer solar cells. *Phys. Chem. Chem. Phys.* 2011, 13, 1970–1983.
[15] Delgado JL, Bouit PA, Filippone S, Herranz MÁ, Martín N. Organic photovoltaics: a chemical approach. *Chem. Commun.* 2010, 46, 4853–4865.
[16] Zhao J, Li Y, Yang G, Jiang K, Lin H, Ade H, Ma W, Yan H. Efficient organic solar cells processed from hydrocarbon solvents. *Nat. Energy* 2016, 1, 15027.
[17] Kirchartz T, Pieters BE, Taretto K, Rau U. Mobility dependent efficiencies of organic bulk heterojunction solar cells: surface recombination and charge transfer state distribution. *Phys. Rev. B* 2009, 80, 035334.
[18] Gross M, Müller DC, Nothofer HG, Scherf U, Neher D, Bräuchle C, Meerholz K. Improving the performance of doped π-conjugated polymers for use in organic light-emitting diodes. *Nature* 2000, 405, 661–665.
[19] Lo MF, Ng TW, Lai S, Fung MK, Lee ST, Lee CS. Stability enhancement in organic photovoltaic device by using polymerized fluorocarbon anode buffer layer. *Appl. Phys. Lett.* 2011, 99, 033302.
[20] Luther JM, Jain PK, Ewers T, Alivisatos AP. Localized surface plasmon resonances arising from free carriers in doped quantum dots. *Nat. Mater.* 2011, 10, 361–366.
[21] Xue M, Shen H, Zhu J, Kim S, Li L, Yu Z, Pei Q, Wang KL, Qasem H, Alzaben AA. Absorption and transport enhancement by Ag nanoparticle plasmonics for organic optoelectronics. In *Electronics, Communications and Photonics Conference (SIECPC), 2011 Saudi International*, 2011, pp. 1–3.
[22] Chen H, Kou X, Yang Z, Ni W, Wang J. Shape-and size-dependent refractive index sensitivity of gold nanoparticles. *Langmuir* 2008, 24, 5233–5237.
[23] Granstrom J, Swensen J, Moon J, Rowell G, Yuen J, Heeger A. Encapsulation of organic light-emitting devices using a perfluorinated polymer. *Appl. Phys. Lett.* 2008, 93, 193304.
[24] Elumalai NK, Uddin A. Open circuit voltage of organic solar cells: an in-depth review. *Energy Environ. Sci.* 2016, 9, 391–410.
[25] Dean C, Young A, Meric I, Lee C, Wang L, Sorgenfrei S, Watanabe K, Taniguchi T, Kim P, Shepard K. Boron nitride substrates for high-quality graphene electronics. *Nat. Nanotechnol.* 2010, 5, 722–726.
[26] Lee C, Wei X, Kysar JW, Hone J. Measurement of the elastic properties and intrinsic strength of monolayer graphene. *Science* 2008, 321, 385–388.
[27] Balandin AA, Ghosh S, Bao W, Calizo I, Teweldebrhan D, Miao F, Lau CN. Superior thermal conductivity of single-layer graphene. *Nano Lett.* 2008, 8, 902–907.
[28] Zhang Y, Tang TT, Girit C, Hao Z, Martin MC, Zettl A, Crommie MF, Shen YR, Wang F. Direct observation of a widely tunable bandgap in bilayer graphene. *Nature* 2009, 459, 820–823.
[29] Mak KF, Sfeir MY, Wu Y, Lui CH, Misewich JA, Heinz TF. Measurement of the optical conductivity of graphene. *Phys. Rev. Lett.* 2008, 101, 196405.
[30] Bae S, Kim H, Lee Y, Xu X, Park JS, Zheng Y, Balakrishnan J, Lei T, Kim HR, Song YI. Roll-to-roll production of 30-inch graphene films for transparent electrodes. *Nat. Nanotechnol.* 2010, 5, 574–578.
[31] Reina A, Jia X, Ho J, Nezich D, Son H, Bulovic V, Dresselhaus MS, Kong J. Large area, few-layer graphene films on arbitrary substrates by chemical vapor deposition. *Nano Lett.* 2008, 9, 30–35.
[32] Kim YD, Kim H, Cho Y, Ryoo JH, Park CH, Kim P, Kim YS, Lee S, Li Y, Park SN. Bright visible light emission from graphene. *Nat. Nanotechnol.* 2015, 10, 676–681.
[33] Gabor NM, Song JC, Ma Q, Nair NL, Taychatanapat T, Watanabe K, Taniguchi T, Levitov LS, Jarillo-Herrero P. Hot carrier-assisted intrinsic photoresponse in graphene. *Science* 2011, 334, 648–652.
[34] Riazimehr S, Bablich A, Schneider D, Kataria S, Passi V, Yim C, Duesberg GS, Lemme MC. Spectral sensitivity of graphene/silicon heterojunction photodetectors. *Solid-State Electron.* 2016, 115, 207–212.
[35] An Y, Behnam A, Pop E, Bosman G, Ural A. Forward-bias diode parameters, electronic noise, and photoresponse of graphene/silicon Schottky junctions with an interfacial native oxide layer. *J. Appl. Phys.* 2015, 118, 114307.
[36] An X, Liu F, Jung YJ, Kar S. Tunable graphene-silicon heterojunctions for ultrasensitive photodetection. *Nano Lett.* 2013, 13, 909–916.
[37] Li X, Zhu H, Wang K, Cao A, Wei J, Li C, Jia Y, Li Z, Li X, Wu D. Graphene-on-silicon Schottky junction solar cells. *Adv. Mater.* 2010, 22, 2743–2748.
[38] Ho PH, Lee WC, Liou YT, Chiu YP, Shih YS, Chen CC, Su PY, Li MK, Chen HL, Liang CT. Sunlight-activated graphene-heterostructure

transparent cathodes: enabling high-performance n-graphene/p-Si Schottky junction photovoltaics. *Energy Environ. Sci.* 2015, 8, 2085–2092.
[39] Xie C, Zhang X, Ruan K, Shao Z, Dhaliwal SS, Wang L, Zhang Q, Zhang X, Jie J. High-efficiency, air stable graphene/Si microhole array Schottky junction solar cells. *J. Mater. Chem. A* 2013, 1, 15348–15354.
[40] Shi E, Li H, Yang L, Zhang L, Li Z, Li P, Shang Y, Wu S, Li X, Wei J. Colloidal antireflection coating improves graphene-silicon solar cells. *Nano Lett.* 2013, 13, 1776–1781.
[41] Chen H, Cao Y, Zhang J, Zhou C. Large-scale complementary macroelectronics using hybrid integration of carbon nanotubes and IGZO thin-film transistors. *Nat. Commun.* 2014, 5, Article ID 4097, Doi: 10.1038/ncomms5097.
[42] Liu J, Wang C, Tu X, Liu B, Chen L, Zheng M, Zhou C. Chirality-controlled synthesis of single-wall carbon nanotubes using vapour-phase epitaxy. *Nat. Commun.* 2012, 3, 1199.
[43] Avouris P, Freitag M, Perebeinos V. Carbon nanotube photonics and optoelectronics. *Nat. Photon.* 2008, 2, 341–350.
[44] Stewart D, Léonard F. Photocurrents in nanotube junctions. *Phys. Rev. Lett.* 2004, 93, 107401.
[45] Aspitarte L, DeBorde T, Sharf T, Kevek J, Minot E. Photothermoelectric effect in suspended semiconducting carbon nanotubes. *Bull. Am. Phys. Soc.* 2014, 59, 216–221.
[46] Lefebvre J, Austing DG, Bond J, Finnie P. Photoluminescence imaging of suspended single-walled carbon nanotubes. *Nano Lett.* 2006, 6, 1603–1608.
[47] Barkelid M, Steele GA, Zwiller V. Probing optical transitions in individual carbon nanotubes using polarized photocurrent spectroscopy. *Nano Lett.* 2012, 12, 5649–5653.
[48] Mueller T, Kinoshita M, Steiner M, Perebeinos V, Bol AA, Farmer DB, Avouris P. Efficient narrow-band light emission from a single carbon nanotube p-n diode. *Nat. Nanotechnol.* 2009, 5, 27–31.
[49] Heller DA, Jin H, Martinez BM, Patel D, Miller BM, Yeung T-K, Jena PV, Höbartner C, Ha T, Silverman SK. Multimodal optical sensing and analyte specificity using single-walled carbon nanotubes. *Nat. Nanotechnol.* 2009, 4, 114–120.
[50] Ma X, Hartmann NF, Baldwin JK, Doorn SK, Htoon H. Room-temperature single-photon generation from solitary dopants of carbon nanotubes. *Nat. Nanotechnol.* 2015, 10, 671–675.
[51] Lee JU, Gipp P, Heller C. Carbon nanotube pn junction diodes. *Appl. Phys. Lett.* 2004, 85, 145–147.
[52] Gabor NM, Zhong Z, Bosnick K, Park J, McEuen PL. Extremely efficient multiple electron-hole pair generation in carbon nanotube photodiodes. *Science* 2009, 325, 1367–1371.
[53] Shi E, Zhang L, Li Z, Li P, Shang Y, Jia Y, Wei J, Wang K, Zhu H, Wu D, Zhang S, Cao A. TiO_2-coated carbon nanotube-silicon solar cells with efficiency of 15%. *Sci. Rep.* 2012, 2. Published online 23 November 2012. Doi: 10.1038/srep00884.
[54] Amer MR, Chang SW, Dhall R, Qiu J, Cronin SB. Zener tunneling and photocurrent generation in quasi-metallic carbon nanotube pn-devices. *Nano Lett.* 2013, 13, 5129–5134.
[55] Jung Y, Li X, Rajan NK, Taylor AD, Reed MA. Record high efficiency single-walled carbon nanotube/silicon p-n junction solar cells. *Nano Lett.* 2012, 13, 95–99.
[56] Perebeinos V, Tersoff, J. Wetting transition for carbon nanotube arrays under metal contacts. *Phys. Rev. Lett.* 2015, 114, 085501.
[57] Perebeinos V, Tersoff, J. Carbon nanotube deformation and collapse under metal contacts. *Nano Lett.* 2014, 14, 4376–4380.
[58] Saito R, Dresselhaus G, Dresselhaus MS. *Physical Properties of Carbon Nanotubes*, vol. 35. World Scientific: Singapore, 1998.
[59] Amer MR, Bushmaker A, Cronin SB. The influence of substrate in determining the band gap of metallic carbon nanotubes. *Nano Lett.* 2012, 12, 4843–4847.
[60] Chang S-W, Hazra J, Amer M, Kapadia R, Cronin SB. A comparison of photocurrent mechanisms in quasi-metallic and semiconducting carbon nanotube pn-junctions. *ACS Nano* 2015, 9, 11551–11556.
[61] Amer M, Chang SW, Cronin SB. Competing photocurrent mechanisms in quasi-metallic carbon nanotube pn devices. *Small* 2015, 11, 3119–3123.
[62] Buscema M, Groenendijk DJ, Steele GA, van der Zant HS, Castellanos-Gomez A. Photovoltaic effect in few-layer black phosphorus PN junctions defined by local electrostatic gating. *Nat. Commun.* 2014, 5, 4651.
[63] Baugher BW, Churchill HO, Yang Y, Jarillo-Herrero P. Optoelectronic devices based on electrically tunable pn diodes in a monolayer dichalcogenide. *Nat. Nanotechnol.* 2014, 9, 262–267.
[64] Jariwala D, Sangwan VK, Wu CC, Prabhumirashi PL, Geier ML, Marks TJ, Lauhon LJ, Hersam MC. Gate-tunable carbon nanotube-MoS_2 heterojunction pn diode. *Proc. Natl. Acad. Sci.* 2013, 110, 18076–18080.
[65] Tsai ML, Su SH, Chang JK, Tsai DS, Chen CH, Wu CI, Li LJ, Chen LJ, He JH. Monolayer MoS_2 heterojunction solar cells. *ACS Nano* 2014, 8, 8317–8322.
[66] Deng Y, Luo Z, Conrad NJ, Liu H, Gong Y, Najmaei S, Ajayan PM, Lou J, Xu X, Ye PD. Black phosphorus-monolayer MoS_2 van der Waals heterojunction p-n diode. *ACS Nano* 2014, 8, 8292–8299.
[67] Lee CH, Lee GH, van Der Zande AM, Chen W, Li Y, Han M, Cui X, Arefe G, Nuckolls C, Heinz TF. Atomically thin p-n junctions with van der Waals heterointerfaces. *Nat. Nanotechnol.* 2014, 9, 676–681.
[68] Jariwala D, Howell S, Chen KS, Kang J, Sangwan VK, Filippone SA, Turrisi R, Marks TJ, Lauhon LJ, Hersam MC. Hybrid, gate-tunable, van der Waals pn heterojunctions from pentacene and MoS_2. *Nano Lett.* 2016, 16, 497–503.
[69] Furchi MM, Pospischil A, Libisch F, Burgdorfer J, Mueller T. Photovoltaic effect in an electrically tunable van der Waals heterojunction. *Nano Lett.* 2014, 14, 4785–4791.
[70] Barone PW, Baik S, Heller DA, Strano MS. Near-infrared optical sensors based on single-walled carbon nanotubes. *Nat. Mater.* 2005, 4, 86–92.
[71] Itkis ME, Borondics F, Yu A, Haddon RC. Bolometric infrared photoresponse of suspended single-walled carbon nanotube films. *Science* 2006, 312, 413–416.
[72] Wang X, Cheng Z, Xu K, Tsang HK, Xu JB. High-responsivity graphene/silicon-heterostructure waveguide photodetectors. *Nat. Photon.* 2013, 7, 888–891.
[73] Ling X, Wang H, Huang S, Xia F, Dresselhaus MS. The renaissance of black phosphorus. *Proc. Natl. Acad. Sci.* 2015, 112, 4523–4530.
[74] Koumoto K, Terasaki I, Funahashi R. Complex oxide materials for potential thermoelectric applications. *MRS Bull.* 2006, 31, 206–210.
[75] Rowe DM. *Thermoelectrics Handbook: Macro to Nano*. CRC Press: Boca Raton, FL, 2005.
[76] Snyder GJ, Toberer, ES. Complex thermoelectric materials. *Nat. Mater.* 2008, 7, 105–114.

[77] Young CD, Hogan T, Schindler J, Iordarridis L, Brazis P, Kannewurf CR, Baoxing C, Uher C, Kanatzidis MG. Complex bismuth chalcogenides as thermoelectrics. In *XVI International Conference on Thermoelectrics, 1997. Proceedings ICT'97*, 1997, pp. 459–462.
[78] Zhao LD, Lo SH, Zhang Y, Sun H, Tan G, Uher C, Wolverton C, Dravid VP, Kanatzidis MG. Ultralow thermal conductivity and high thermoelectric figure of merit in SnSe crystals. *Nature* 2014, 508, 373–377.
[79] Dresselhaus M, Dresselhaus G, Sun X, Zhang Z, Cronin S, Koga T. Low-dimensional thermoelectric materials. *Phys. Solid State* 1999, 41, 679–682.
[80] Lv H, Lu W, Shao D, Sun Y. Large thermoelectric power factors in black phosphorus and phosphorene. *arXiv preprint arXiv:1404.5171,* 2014.
[81] Fei R, Faghaninia A, Soklaski R, Yan JA, Lo C, Yang L. Enhanced thermoelectric efficiency via orthogonal electrical and thermal conductances in phosphorene. *Nano Lett.* 2014, 14, 6393–6399.
[82] Flores E, Ares JR, Castellanos-Gomez A, Barawi M, Ferrer IJ, Sánchez C. Thermoelectric power of bulk black-phosphorus. *Appl. Phys. Lett.* 2015, 106, 022102.
[83] Liao BL, Zhou JW, Qiu B, Dresselhaus MS, Chen G. Ab initio study of electron-phonon interaction in phosphorene. *Phys. Rev. B* 2015, 91, 235419.
[84] Buscema M, Barkelid M, Zwiller V, van der Zant HS, Steele GA, Castellanos-Gomez A. Large and tunable photothermoelectric effect in single-layer MoS_2. *Nano Lett.* 2013, 13, 358–363.
[85] Yan RS, Simpson JR, Bertolazzi S, Brivio J, Watson M, Wu XF, Kis A, Luo TF, Walker ARH, Xing HG. Thermal conductivity of monolayer molybdenum disulfide obtained from temperature-dependent Raman spectroscopy. *ACS Nano* 2014, 8, 986–993.
[86] Mak KF, Lee C, Hone J, Shan J, Heinz TF. Atomically thin MoS_2: a new direct-gap semiconductor. *Phys. Rev. Lett.* 2010, 105, 136805.
[87] Wickramaratne D, Zahid F, Lake RK. Electronic and thermoelectric properties of few-layer transition metal dichalcogenides. *J. Chem. Phys.* 2014, 140, 124710.
[88] Wen H. Theoretical investigations of thermoelectric effects in advanced low dimensional materials. PhD Thesis, 2014.
[89] Li W, Carrete J, Mingo N. Thermal conductivity and phonon linewidths of monolayer MoS_2 from first principles. *Appl. Phys. Lett.* 2013, 103, 253103.
[90] Yavorsky BY, Hinsche N, Mertig I, Zahn P. Electronic structure and transport anisotropy of Bi_2Te_3 and Sb_2Te_3. *Phys. Rev. B* 2011, 84, 165208.
[91] Liu W, Lukas KC, McEnaney K, Lee S, Zhang Q, Opeil CP, Chen G, Ren Z. Studies on the Bi_2Te_3-Bi_2Se_3-Bi_2S_3 system for mid-temperature thermoelectric energy conversion. *Energy Environ. Sci.* 2013, 6, 552–560.
[92] Goyal V, Teweldebrhan D, Balandin AA. Mechanically-exfoliated stacks of thin films of Bi_2Te_3 topological insulators with enhanced thermoelectric performance. *Appl. Phys. Lett* 2010, 97, 133117.
[93] Tan M, Deng Y, Hao Y. Enhanced thermoelectric properties and superlattice structure of a Bi_2Te_3/ZrB_2 film prepared by ion-beam-assisted deposition. *J. Phys. Chem. C* 2013, 117, 20415–20420.
[94] Greenaway DL, Harbeke G. Band structure of bismuth telluride, bismuth selenide and their respective alloys. *J. Phys. Chem. Solids* 1965, 26, 1585–1604.
[95] Wickramaratne D, Zahid F, Lake RK. Electronic and thermoelectric properties of van der Waals materials with ring-shaped valence bands. *J. Appl. Phys.* 2015, 118, 075101.
[96] Qin GZ, Yan QB, Qin ZZ, Yue SY, Hu M, Su G. Anisotropic intrinsic lattice thermal conductivity of phosphorene from first principles. *Phys. Chem. Chem. Phys.* 2015, 17, 4854–4858.
[97] Fei RX, Faghaninia A, Soklaski R, Yan JA, Lo C, Yang L. Enhanced thermoelectric efficiency via orthogonal electrical and thermal conductances in phosphorene. *Nano Lett.* 2014, 14, 6393–6399.
[98] Jain A, McGaughey AJH. Strongly anisotropic in-plane thermal transport in single-layer black phosphorene. *Sci. Rep.* 2015, 5. Available from: http://www.nature.com/articles/srep08501.
[99] Zhang J, Liu H, Cheng L, Wei J, Liang J, Fan D, Shi J, Tang X, Zhang Q. Phosphorene nanoribbon as a promising candidate for thermoelectric applications. *Sci. Rep.* 2014, 4, 2014.
[100] Kou LZ, Chen CF, Smith SC. Phosphorene: fabrication, properties, and applications. *J. Phys. Chem. Lett.* 2015, 6, 2794–2805.
[101] Vining CB. An inconvenient truth about thermoelectrics. *Nat. Mater.* 2009, 8, 83–85.
[102] Kim HS, Liu W, Chen G, Chu CW, Ren Z. Relationship between thermoelectric figure of merit and energy conversion efficiency. *Proc. Natl. Acad. Sci.* 2015, 112, 8205–8210.

Bionotes

Moh R. Amer
Center of Excellence for Green Nanotechnologies, Department of Electrical Engineering, University of California, Los Angeles, CA 90095, USA; and Center of Excellence for Green Nanotechnologies, Department of Electrical Engineering, King Abdulaziz City for Science and Technology, Riyadh 11442, Saudi Arabia,
mamer@seas.ucla.edu

Moh R. Amer currently serves as the co-director of the Center of Excellence for Green Nanotechnologies (CEGN) at University of California, Los Angeles (UCLA), and King Abdulaziz City for Science and Technology (KACST). CEGN serves as a collaborative multimillion-dollar research center between KACST and UCLA, which aims in finding emerging clean and sustainable energy technologies. He is also an assistant professor at KACST where he is the principal investigator of various technical projects. Prior to his appointments at UCLA and KACST, Dr. Amer served as a research associate in the Center of Energy Nanoscience at University of Southern California (USC), part of U.S. Department of Energy, U.S. Office of Basic Energy Sciences, and U.S. Energy Frontier Research Center. His previous work involves the investigation of the electronic transport of carbonaceous devices such as carbon nanotubes, high-frequency devices using nanomaterials, phonon and thermal transport of nanoscale devices, and nanoelectromechanical resonator structures. His research group focuses on low-dimensional devices such as graphene and 2D materials for industrial applications, including electronic switches and high-frequency devices, optoelectronic and photonic devices for various sensing applications, and thermoelectric devices for power-generation applications. Dr. Amer is the

recipient of several grant awards, including National Academy of Science Arab-American Frontiers seed grant fellowship. Dr. Amer has authored and co-authored many scientific papers. He is currently a fellow of the American Chemical Society and the American Physical Society.

Yazeed Alaskar
Center of Excellence for Green Nanotechnologies, Department of Electrical Engineering, University of California, Los Angeles, CA 90095, USA; and Center of Excellence for Green Nanotechnologies, Department of Electrical Engineering, King Abdulaziz City for Science and Technology, Riyadh 11442, Saudi Arabia

Yazeed Alaskar is a PhD candidate at the Department of Electrical Engineering, University of California, Los Angeles (UCLA). He received his bachelor's degree in electrical engineering from King Saud University, Saudi Arabia, in 2006. In 2011, he received his master's degree in electrical engineering from University of Michigan-Ann Arbor. In September 2011, he joined the Device Research Laboratory at Electrical Engineering Department of UCLA, pursuing his PhD degree under the supervision of Professor Kang L. Wang. His current research topics involve the growth of III-V semiconductors on van der Waals materials, and related heterostructures using molecular beam epitaxy. He is also interested in optoelectronic devices and energy-harvesting devices.

Hussam Qasem
Center of Excellence for Green Nanotechnologies, Department of Electrical Engineering, University of California, Los Angeles, CA 90095, USA; and Center of Excellence for Green Nanotechnologies, Department of Electrical Engineering, King Abdulaziz City for Science and Technology, Riyadh 11442, Saudi Arabia

Hussam Qasem is a PhD student in the Electrical Engineering Department at UCLA, and a researcher at both the Device Research Lab (DRL) and the CEGN. His current focus is on nano-electronic devices based on atomically thin materials. Hussam had obtained his master's degree from UCLA in 2014, where he worked on organic photovoltaics (OPVs) and inverted OPVs. Hussam obtained his BSc degree from King Abdulaziz University in electric power systems engineering. Following graduation, Hussam joined KACST as a researcher where he worked on reactive power compensation systems, and helped enhance the tracking systems for solar panels.

Fadhel Alsaffar
Center of Excellence for Green Nanotechnologies, Department of Electrical Engineering, King Abdulaziz City for Science and Technology, Riyadh 11442, Saudi Arabia

Fadhel Alsaffar is a researcher at CEGN at King Abdulaziz City for Science and Technologies. He received his bachelor's degree in mechanical engineering from King Fahd University of Petroleum and Minerals.

Abdulrahman Alhussain
Center of Excellence for Green Nanotechnologies, Department of Electrical Engineering, King Abdulaziz City for Science and Technology, Riyadh 11442, Saudi Arabia

Abdulrahman Alhussain is a researcher at the CEGN, a center affiliated with both UCLA and KACST. Abdulrahman obtained his bachelor's degree in 2014 from King Saud University, located in Riyadh, Saudi Arabia, in electronics engineering. His current research interests include studying the electronic properties of low-dimensional materials for the next generation of electronics.